OPEN

Electrostatic Induced Stretch Growth of Homogeneous β-Ni(OH)$_2$ on Graphene with Enhanced High-Rate Cycling for Supercapacitors

Zhong Wu[1,2], Xiao-Lei Huang[1], Zhong-Li Wang[1], Ji-Jing Xu[1], Heng-Guo Wang[1] & Xin-Bo Zhang[1]

[1]State Key Laboratory of Rare Earth Resource Utilization, Changchun Institute of Applied Chemistry, Chinese Academy of Sciences, Changchun 130022, China, [2]University of Chinese Academy of Sciences, Beijing 100124, China.

Supercapacitors, as one of alternative energy devices, have been characterized by the rapid rate of charging and discharging, and high power density. But they are now challenged to achieve their potential energy density that is related to specific capacitance. Thus it is extremely important to make such materials with high specific capacitances. In this report, we have gained homogenous Ni(OH)$_2$ on graphene by efficiently using of a facile and effective electrostatic induced stretch growth method. The electrostatic interaction triggers advantageous change in morphology and the ordered stacking of Ni(OH)$_2$ nanosheets on graphene also enhances the crystallization of Ni(OH)$_2$. When the as-prepared Ni(OH)$_2$/graphene composite is applied to supercapacitors, they show superior electrochemical properties including high specific capacitance (1503 F g^{-1} at 2 mV s^{-1}) and excellent cycling stability up to 6000 cycles even at a high scan rate of 50 mV s^{-1}.

Supercapacitors (SCs), also known as ultracapacitors or electrochemical capacitors, have attracted numerous attentions for energy storage due to their high power performance, long cycle life, and low maintenance cost[1–3]. In general, SCs can be classified into electrical double layer capacitors (EDLCs) and pseudocapacitors based on their energy storage mechanisms[4–6]. EDLCs store the charge using reversible adsorption and desorption of the electrolyte ions onto the surface of active materials. EDLCs, mainly based on carbon materials, that are electrochemically stable and physical processes, hence they can perform ultrahigh power density and excellent cycle life, yet their further applications are confined by the limited energy density[7–10]. On the contrary, pseudocapacitors based on fast reversible surface redox reactions hold the potential of much higher energy density[11–14]. Although extensive studies have been made, there is still an urgent demand for pseudocapacitors that allow for fast charging and discharging with high stability for the storage of electrical energy in practical application[15–19].

Recently, two-dimensional nanomaterials, which possess nanoscale dimension in thickness and infinite length in the plane, have attracted tremendous attention owing to their unique properties and potential applications in the areas of energy storage and conversion such as supercapacitors[20–22]. Ni(OH)$_2$, with unique layer structure has been developed for pseudocapacitive applications[23–26]. However, its practical application in SCs is still hindered by the poor conductivity of Ni(OH)$_2$. To address this problem, downsizing it to nanoscale and constructing hybrid materials with highly electrical conductive, flexible, and chemically stable conductive substrates have been investigated to be promising approaches[27–30]. Graphene, emerging as a 2D single layer of carbon atoms with a hexagonal packed structure, has attracted considerable attention in scientific researches as conductive substrate due to its ultrahigh surface area ($\sim$2630 m^2 g^{-1} for single-layer graphene), low cost, and high electrical conductivity (10^3–10^4 S m^{-1})[31–36]. Graphene can be obtained through reduction of graphene oxide (GO) obtained by modified Hummer's methods. It is an inexpensive processes, which is currently used for large-scale production of graphene[37,38]. Typically, GO contains carboxylic acid, epoxy, and hydroxyl groups and these unique features make it an excellent 2D support to load Ni(OH)$_2$ and then improving the electrochemical properties of Ni(OH)$_2$[39–43]. However, there is still a great challenge to reduce aggregation-derived degradation in capacitance especially at a high scan rate associated with untight contact between graphene nanosheets and metal hydroxide.
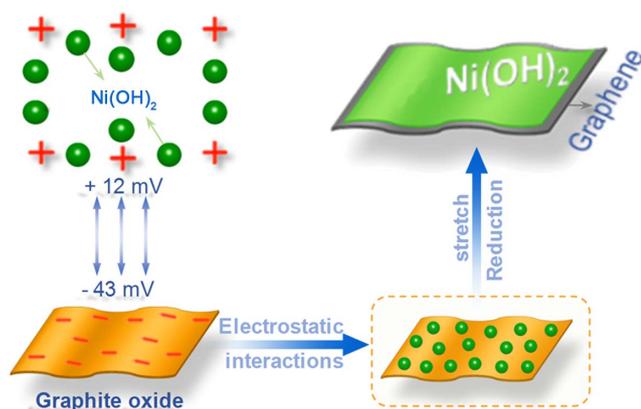
Figure 1 | Formation mechanism. Schematic illustration of $Ni(OH)_2$ stretch growth on graphene.

Herein, we report a facile electrostatic induced stretch growth method to achieve homogenous coating of $Ni(OH)_2$ nanosheets on graphene under mild reflux condition. The electrostatic interaction triggers advantageous change in morphology and the ordered stacking of $Ni(OH)_2$ nanosheets on graphene, and also enhances the crystallization of $Ni(OH)_2$. Functional groups of GO (hydroxyl, epoxy, carboxyl and carbonyl groups) act as anchor sites for in-situ growth. The combined advantages of unique structure, high conductivity and structural stability endow the as-prepared composite ($Ni(OH)_2$/GS) with superior performances including high specific capacitance (1503 F g^{-1} at 2 mV s^{-1}) and excellent cycling stability up to 6000 cycles even at a high scan rate of 50 mV s^{-1}.

Results

Morphology and structure analysis. Figure 1 shows the formation procedure of homogenous coating of precursor $Ni(OH)_2$ on graphene under mild reflux condition. First, precursor $Ni(OH)_2$ is obtained by facile precipitation reaction. Then, precursors are deposited onto the surface of GO. The Zeta potential of precursor $Ni(OH)_2$ and GO are measured under reaction condition by dynamic light scattering. The precursor $Ni(OH)_2$ is positively charged (+12 mV) and GO are negatively charged (−43 mV). With the help of electrostatic interacting between reverse charged reactants, $Ni(OH)_2$ is anchored onto the surface of GO nanosheets. Thereafter, $Ni(OH)_2$/GS composites are obtained after reflux in DMF at 95°C for 16 h. Different $Ni(OH)_2$/GS composites are prepared by control the mass ratio of GO to $Ni(OH)_2$ as 1 : 20, 1 : 5, and 1 : 2, and the corresponding composites are denoted as $Ni(OH)_2$/GS-20, $Ni(OH)_2$/GS-5, and $Ni(OH)_2$/GS-2, respectively. For comparison, pure $Ni(OH)_2$ is also synthesized under the similar conditions except for the absence of graphene.

The crystal structures of the obtained samples are characterized by X-ray diffraction (XRD) pattern. As shown in Figure 2a, all the diffraction peaks of the precursor $Ni(OH)_2$, pure $Ni(OH)_2$, and $Ni(OH)_2$/GS composites can be indexed to beta-$Ni(OH)_2$ (JCPDS: 14-0117). The 2θ degrees for diffractions of (001), (100), (101), (102), (110), and (111) planes are at 19.258, 33.064, 38.541, 52.100, 59.052, and 62.726°, respectively. For precursor $Ni(OH)_2$ and pure $Ni(OH)_2$, the XRD diffraction peaks are low and broad, revealing the poor crystallinity and small size of crystallite. Interestingly, with the presence of graphene, the diffraction peaks become obviously stronger, indicating the enhanced crystallization of the $Ni(OH)_2$/GS. To further confirm the contribution of graphene, we also investigated other composites with different mass ratio of GO to $Ni(OH)_2$. With the addition of GO, it can be found that the crystallization can be optimized with increasing amount of GO, as is displayed by the XRD patterns of $Ni(OH)_2$/GS-20, $Ni(OH)_2$/GS-5, and $Ni(OH)_2$/GS-2 in

Figure 2b. These results show the existence of graphene can enhance the crystallization of $Ni(OH)_2$.

The morphology and structure of precursor $Ni(OH)_2$, pure $Ni(OH)_2$, and $Ni(OH)_2$/GS composites are studied by field emission scanning electron microscopy (FESEM) and transmission electron microscopy (TEM). As shown in Figure S1, precursor $Ni(OH)_2$ is stacked particle and the obtained pure $Ni(OH)_2$ is observed as aggregated nanoplate. Figure 3a and b display the morphology and structure of $Ni(OH)_2$/GS-20 composite, we can also observe stacked particles of $Ni(OH)_2$ with low mass ratio of graphene substrates. The morphology and structure of $Ni(OH)_2$/GS-5 and $Ni(OH)_2$/GS-2 composites are shown in Figure 3c–f, respectively. Interestingly, it is found that $Ni(OH)_2$ and graphene are so much alike that it is impossible to discriminate one from the other, which indicates that $Ni(OH)_2$ and graphene are homogenously contacted and intercalated with each other (vide infra). Moreover, the graphene sheets overlap with each other and thus result in a three-dimensional and porous network. Combined with the results from XRD patterns, it can be speculated that the functional groups between graphene sheets chelate $Ni(OH)_2$ disordered stacks with the help of electrostatic interaction. And then these groups can act as anchoring sites, enabling $Ni(OH)_2$ stretch on graphene sheets and forming ordered stack on interfaces of graphene sheets, which is depicted in Figure S2.

The high-resolution TEM image of $Ni(OH)_2$/GS-5 in Figure 4a shows lattice fringes of 0.27 and 0.23 nm, which are consistent to the d spacing of the (100) and (101) planes of $Ni(OH)_2$, confirming its crystalline nature in accordance with the XRD results. Furthermore, the distribution of graphene and $Ni(OH)_2$ in the $Ni(OH)_2$/GS-5 composite is then analyzed using energy dispersive X-ray (EDX) spectroscopy mapping technique (Figure 4b–e). The region of nickel (Ni), oxygen (O), and carbon (C) is similar to the selected area in Figure 4b. These results clearly show that the elements of Ni, O, and C are distributed homogeneously, further indicating that the coating of $Ni(OH)_2$ on graphene is uniform and complete.

X-ray photoelectron spectroscopy (XPS) technique is employed to analyze the chemical state of all elements in $Ni(OH)_2$/GS-5 composite (Figure 5a–d). As shown in Figure 5a, the survey spectrum of $Ni(OH)_2$/GS-5 also certify the presence of Ni, O, and C in the composite, which is consistent with the above FESEM and EDX results. Figure 5b shows the deconvolution of C 1 s spectrum with different oxygen containing functional groups, including the non-oxygenated C in C-C at 284.5 eV, the carbon in C-O at 286.4 eV, and the carbon in C=O at 288.8 eV. These hydrophilic functional groups in $Ni(OH)_2$/GS-5 are believed to play dual roles here. On the one hand, these hydrophilic groups can enhance the wettability of the electrode and further improve the compatibility between the electrode and the electrolyte. On the other hand, these groups can act as anchoring sites to interact with precursors, enabling $Ni(OH)_2$ to directly grow on graphene sheets. The peaks of the Ni 2p spectrum in Figure 5c can be assigned to the Ni $2p_{3/2}$ (850–865 eV) and Ni $2p_{1/2}$ (870–885 eV) spin orbit levels, which show Ni ion is +2 valence state. Figure 5d shows the deconvolution of O 1 s spectrum with three peaks. The peak at 530.2 eV is ascribed to C-O-Ni bond. The peak at 531.2 eV is assigned to C=O groups or shoulder peak of O 1 s in $Ni(OH)_2$, and the peak at 533.1 eV is ascribed to C-OH and/or C-O-C groups (hydroxyl and/or epoxy). Raman spectra of the $Ni(OH)_2$/GS-5 composites before and after reduction are shown in Figure 5e and f. There are two prominent peaks at 1357 and 1595 cm^{-1}, which correspond to the D and G bands of carbon in the $Ni(OH)_2$/GS-5 composite before reflux treatment. For $Ni(OH)_2$/GS-5 composite, the peaks for D and G bands are 1356 and 1600 cm^{-1}, respectively. The G band shifts in carbon-based composites relate to the charge transfer between the carbon and other compounds. Therefore, the observed shift by 6 cm^{-1} indicates the presence of a charge transfer from graphene to $Ni(OH)_2$. These intimate bindings afford facile electron transports through $Ni(OH)_2$ to graphene, and further facilitates

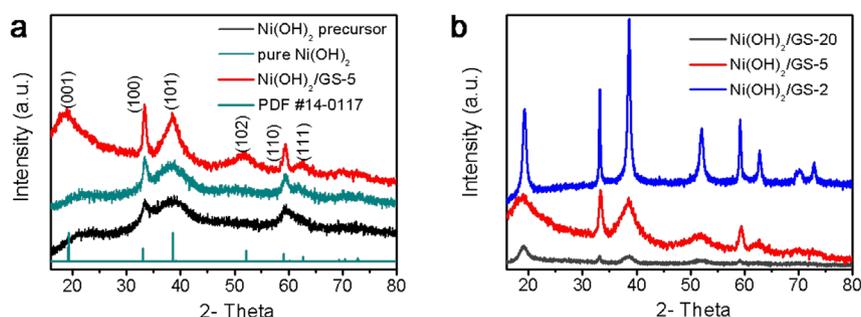**Figure 2 | Sample characterizations of the samples.** (a) XRD patterns of precursor $Ni(OH)_2$, pure $Ni(OH)_2$ and the $Ni(OH)_2$/GS-5 composite. (b) XRD patterns of the $Ni(OH)_2$/GS composites.

electrons to the current collectors, leading to low electrical resistances. In addition, the N_2-adsorption-desorption isotherm and the pore-size distribution of $Ni(OH)_2$/GS-5 composite and pure $Ni(OH)_2$ are collected in Figure S3a and b. The actual mass ratio of graphene in $Ni(OH)_2$/GS-5 composite after reflux treatment is determined by thermogravimetric analysis in Figure S3c to be 10 wt%.

Electrochemical measurements. Cyclic voltammetry (CV) is then employed to investigate the capacitance mechanism and the specific capacitances at various scan rates. Figure 6a and b show CV curves of $Ni(OH)_2$/GS-5 and pure $Ni(OH)_2$ electrodes from 2 to 200 mV s^{-1}, respectively. The two strong peaks indicate that the capacitive behavior mainly results from pseudocapacitive capacitance based on redox mechanism. The positive peak observed at 0.42 V (vs Hg/HgO) could be reasonably attributed to the following reaction: $Ni(II) \rightarrow Ni(III)$, indicating an oxidation process. And the corresponding negative peak occurs at 0.30 V (vs Hg/HgO), indicating a reduction process: $Ni(III) \rightarrow Ni(II)$. The specific capacitances can be calculated by integrating the area under the CV curves (see supplementary information for details). The average specific capacitances of $Ni(OH)_2$/GS-5 and pure $Ni(OH)_2$ electrodes are calculated to be 1503 and 1064 F g^{-1} at the scan rate of 2 mV s^{-1}, which are shown in Figure 6c. For $Ni(OH)_2$/GS-5 electrodes,

interestingly, CV curves are found to retain a similar shape to that of a scan rate of 2 mV s^{-1} even at 200 mV s^{-1}. Although the specific capacitances decrease with the increasing scan rates, a high value of 299 F g^{-1} can still be obtained at 200 mV s^{-1}. However, a lower value of 142 F g^{-1} is obtained at 200 mV s^{-1} for pure $Ni(OH)_2$ electrodes. In addition to CV curves, galvanostatic discharge curves (GC) (Figure S4) are also employed to estimate the specific capacitance, which are shown in supplementary information. The enhanced performance of $Ni(OH)_2$/GS-5 can be attributed to the improved electrical conductivity and facilitated ion transport and diffusion rate. It can be explained according to Figure 6d, where illustrates the relationship between anodic peak current and square root of scan rates for $Ni(OH)_2$/GS-5 and pure $Ni(OH)_2$ electrode. Note that the anodic peak current (i) increase linearly with square root of scan rates ($v_{1/2}$), which satisfies Cottrell equation and indicates a diffusion-controlled process. According to Cottrell equation, $i = nFACD_{1/2}/(\pi t)_{1/2}$, where n is the number of electrons transferred during the redox reaction, F is a faradic constant, A is the effective surface area of the working electrode, C is the concentration of the electrolyte, D is the diffusion coefficient and Cottrell equation can be simplified as $i = a \ v_{1/2}$[43] We can conclude that the anodic peak current (i) increases with square root of the diffusion coefficient (D) in the certain situation. From Figure 6d, we can find that the $Ni(OH)_2$/GS-5 composite represents fast diffusion velocity.

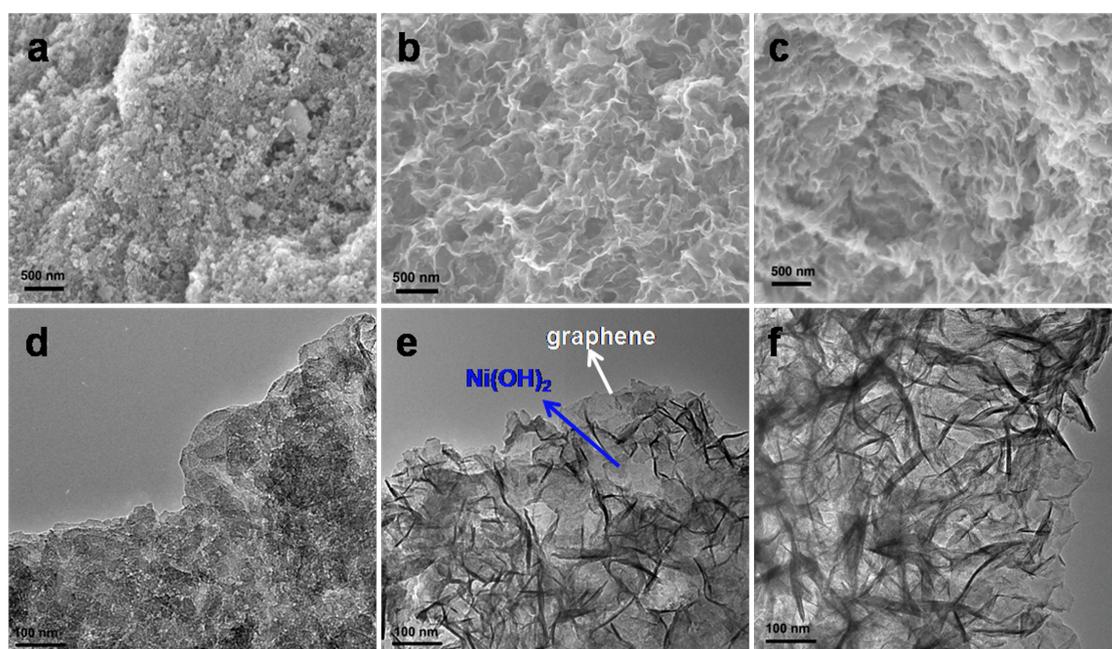**Figure 3 | Sample characterizations of the samples.** FESEM and TEM images of (a, b) $Ni(OH)_2$/GS-20, (c, d) $Ni(OH)_2$/GS-5, and (e, f) $Ni(OH)_2$/GS-2 composites.
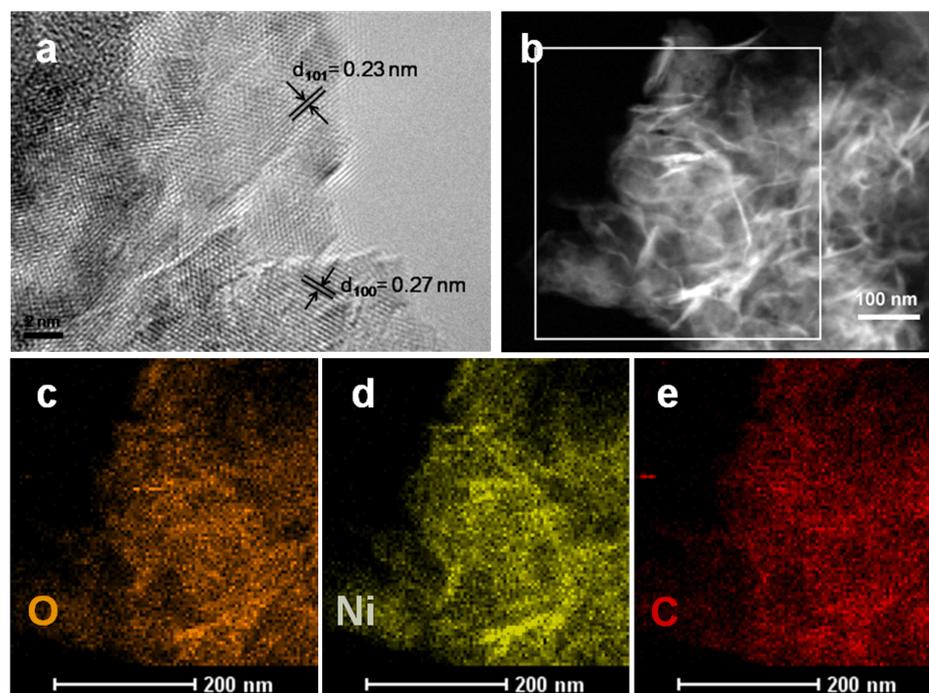
Figure 4 | Sample characterizations of the samples. (a) High resolution TEM image and (b) STEM image of Ni(OH)$_2$/GS-5 composite and corresponding elemental mapping images of (c) oxygen (d) nickel and (e) carbon in the selected area (white rectangle in (b)).

Figure 5 | Sample characterizations of the Ni(OH)$_2$/GS-5 composite. (a) The survey XPS spectrum, (b) Deconvolution of C 1 s spectrum, (c) Ni 2p spectrum of Ni(OH)$_2$/GS-5, and (d) Deconvolution of O 1 s spectrum, (e) Raman spectra of the Ni(OH)$_2$/GO, and (e) Raman spectra of the Ni(OH)$_2$/GS.

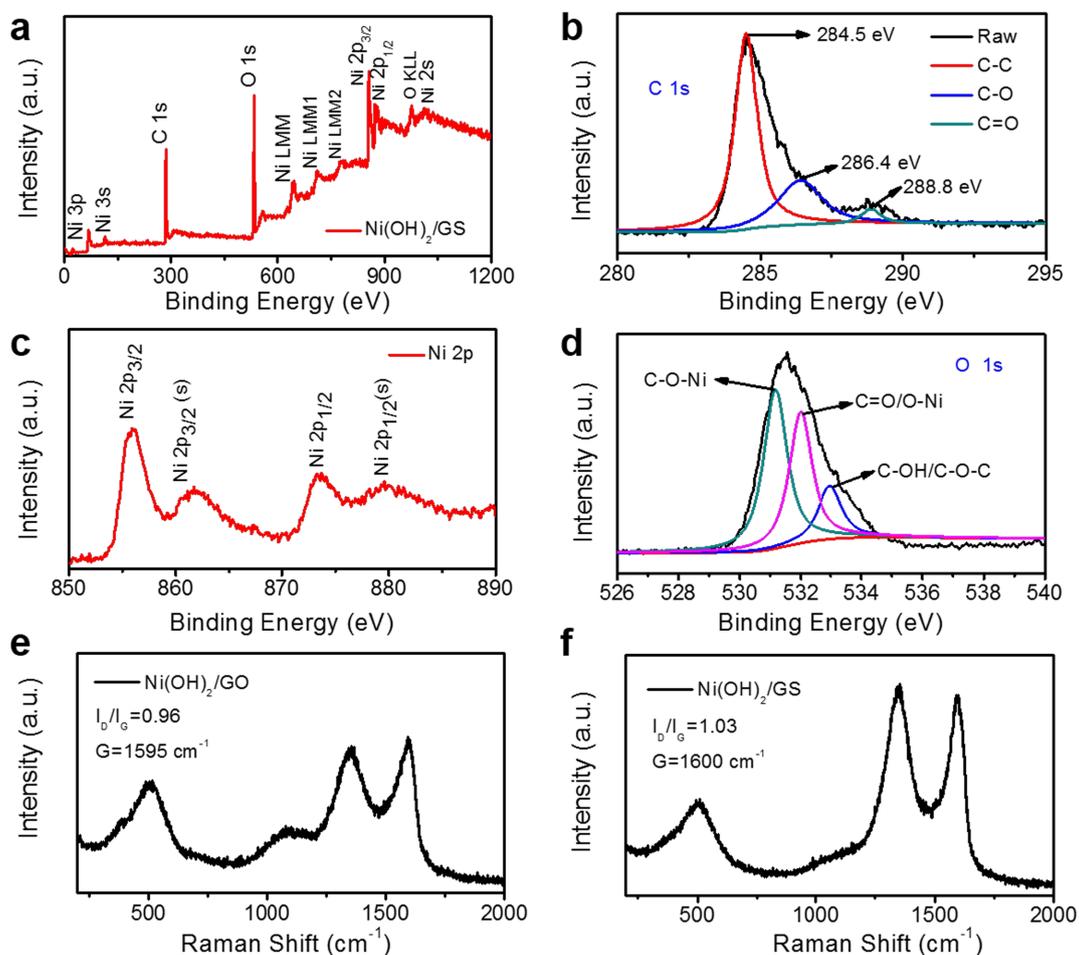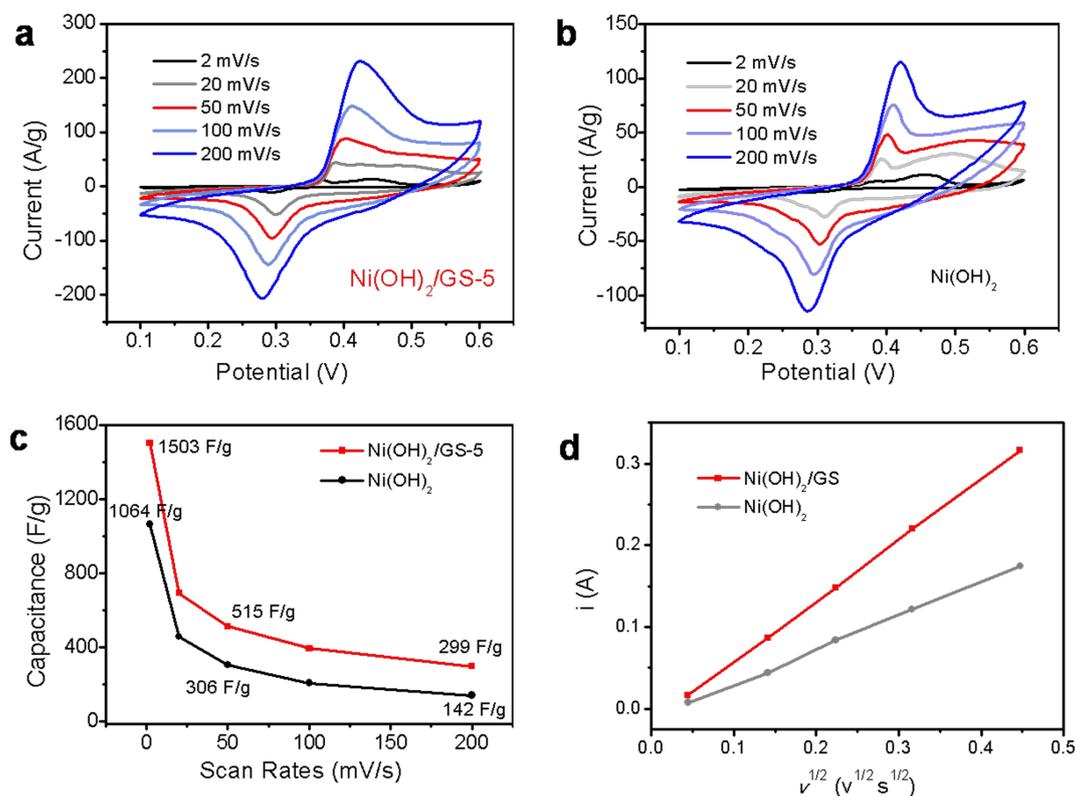**Figure 6 | Electrochemical properties of Ni(OH)$_2$/GS-5 and pure Ni(OH)$_2$.** (a) CV curves of Ni(OH)$_2$/GS-5, (b) CV curves of pure Ni(OH)$_2$, (c) Average specific capacitances of Ni(OH)$_2$/GS-5 and pure Ni(OH)$_2$ at various scan rates, (d) Relationship between anodic peak current and square root of scan rates for Ni(OH)$_2$/GS-5 and pure Ni(OH)$_2$ electrode.

For comparison, the electrochemical properties of other composites with different mass ratios of GO to Ni(OH)$_2$ are also measured by galvanostatic discharge curves (GC) and CV curves, as shown in Figure S5. Table S1 and S2 summarize the specific capacitances of Ni(OH)$_2$/GS-20, Ni(OH)$_2$/GS-5, Ni(OH)$_2$/GS-2 composites and pure Ni(OH)$_2$ calculated from CV curves and galvanostatic discharge curves. Graphene prevents the aggregation of Ni(OH)$_2$ nanosheets, which enables an effective redox reaction at the interface of Ni(OH)$_2$ and electrolyte. Besides, the oxygen-containing functional groups enhance the wettability of the electrode and thereby the electroactive species, Ni(OH)$_2$, can be easily infiltrated by electrolyte ions for charge-transfer reactions. It can be noted that insufficient and excess graphene are harmful for the improved performance. For Ni(OH)$_2$/GS-20, excess Ni^{2+} ions around GO prevent themself from dispersing on GO nanosheets well thus resulting in low capacitance with a capacitance of 1052 F g^{-1} at 2 mV s^{-1}. On the other hand, too many graphene in Ni(OH)$_2$/GS-2 induce the aggregation of graphene sheets and the lower capacitance of graphene ascribe to EDLC behavior compromise the capacitance based on the total mass of the composite. The highest capacitance of Ni(OH)$_2$/GS-2 is 1334 F g^{-1} at 2 mV s^{-1}. The optimal ratio of GO to Ni(OH)$_2$ is 1 : 5 by mass.

Discussion

Figure 7a shows CV curves of Ni(OH)$_2$/GS-5, pure Ni(OH)$_2$, and Ni foam at a scan rate of 50 mV s^{-1}. Note that the background signal deriving from Ni foam is negligible. The average specific capacitance of the Ni(OH)$_2$/GS-5 at a scan rate of 50 mV s^{-1} is 515 F g^{-1}, a factor of ~1.7 higher than that of pure Ni(OH)$_2$ at the same scan rate. For practical application, cyclic stability is crucial for an electrode material in electrochemical capacitors. As shown in Figure 7b, the loss in capacity for Ni(OH)$_2$/GS-5 is only 3.5% within 6000 cycles (from 515 to 497 F g^{-1}). In general, the excellent cycling stability is attributed

the intimate bindings of Ni(OH)$_2$ nanosheets and graphene nanosheets affording facile electron transports through Ni(OH)$_2$ to graphene, and further facilitating electrons to the current collectors, which can improve their electronic and ionic conductivities. Besides, it should be noted that a decrease can be found before 2000 cycles and there is a slight increase with the cycles ranging from 2000 to 4000 cycles and then the tendency holds nearly stable after 4000 cycles. Taking the properties of the composite into account, the slight increase may be attributed to the improvement of ion accessibility owing to the functional groups on graphene which have been confirmed by previous XPS results (Figure 5).

To further analyze the reason that Ni(OH)$_2$/GS-5 composite performs more excellent capacitive behavior than pure Ni(OH)$_2$, the transport characteristics of the charge carriers within electrode are investigated using electrochemical impedance spectroscopy (EIS) as shown in Figure 7c. Nyquist plots are composed by two distinct parts, a semicircle at high frequency and a linear line at low frequency. The high frequency semicircle intercepts the real axis at R_s and ($R_s + R_{ct}$), while R_s means a bulk solution resistance and R_{ct} means a charge-transfer resistance, respectively. R_s is related with several parts including the electrolyte resistance, the collector/electrode contact resistance, and the electrode/electrolyte interface resistance. But the morphological difference has little effect on the ohmic resistance of the supercapacitor device, as shown in the zoom-in of the intersection part. We can note that there is no obvious distinction between Ni(OH)$_2$/GS-5 and pure Ni(OH)$_2$ electrode with regard to R_s. In terms of R_{ct}, the radius of the semicircle is about 0.5 ohm, which is smaller than that of pure Ni(OH)$_2$ (about 1 ohm), suggesting the lower charge-transfer resistance. We can assume that synergistic effects between Ni(OH)$_2$ and graphene are favorable to the penetration of electrolytes into the whole electrode matrix and then reduce electrical resistance at the interface between the electrode material and the current collector. The inclined portion of the curve (about
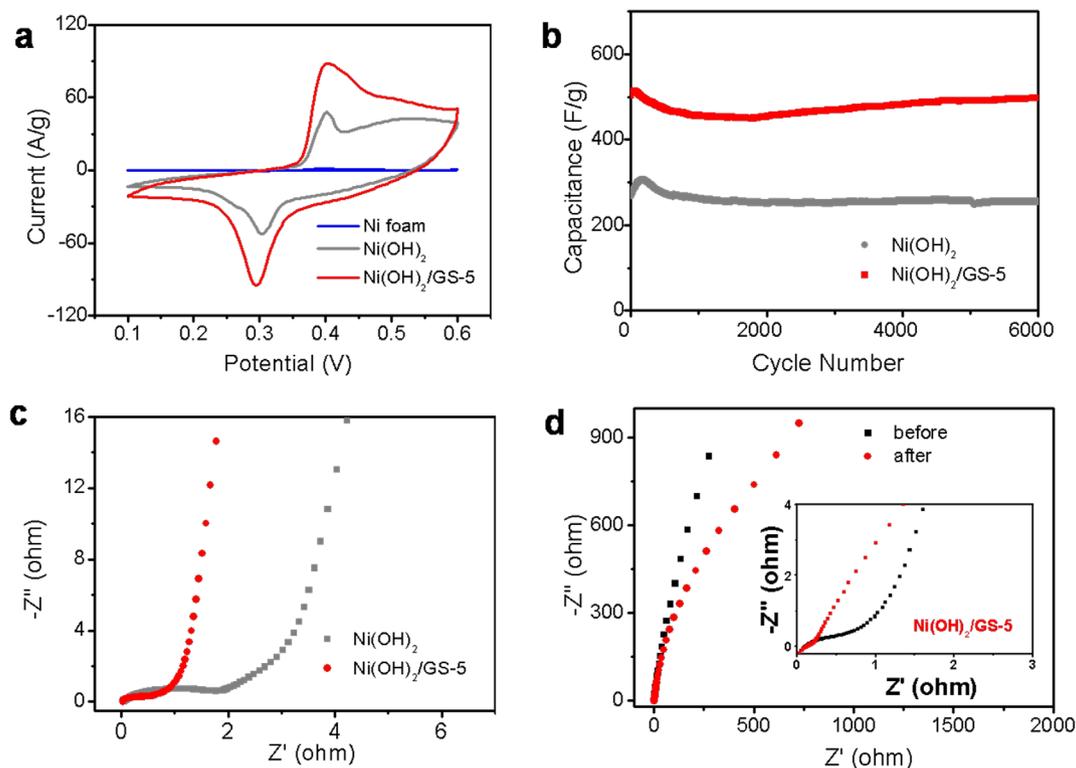
Figure 7 | Electrochemical properties of Ni(OH)$_2$/GS-5 and pure Ni(OH)$_2$. (a) CV curves of Ni(OH)$_2$/GS-5, pure Ni(OH)$_2$ and Ni foam at a scan rate of 50 mV s^{-1}, (b) Cycling stability of Ni(OH)$_2$/GS-5 and pure Ni(OH)$_2$ at 50 mV s^{-1}, (c) EIS data of Ni(OH)$_2$/GS-5 and pure Ni(OH)$_2$ before cycling, (c) EIS data of Ni(OH)$_2$/GS-5 before and after 6000 cycles. (Inset is the enlarged plots).

45°) in the low frequency is ascribed to the Warburg impedance, which is related to ion diffusion/transport in the electrolyte. The more vertical shape at low frequency for Ni(OH)$_2$/GS-5 indicates a more capacitive behavior of the electrode.

Figure 7d shows the EIS data of Ni(OH)$_2$/GS-5 composite before and after 6000 cycles. In terms of R_{ct}, the value after 6000 cycles is about 0.2 ohm, a lower resistance than the previous result. It may be attributed to the improvement of ion accessibility resulting from the increased wettability during the cycling process, which provides an evidence for the trend of cycling stability in Figure 6b. However, we can find that there is a little deviation from a vertical line in terms of the inclined portion of the curve in the low frequency after 6000 cycles, indicating the lack of good ion diffusion/transport in the electrolyte to the electrode surface.

In summary, we have developed a facile and effective stretch growth technique for homogenous coating Ni(OH)$_2$ on graphene to tackle the challenges of pseudocapacitor materials in SCs. The electrostatic interaction triggers advantageous change in morphology and the ordered stacking of Ni(OH)$_2$ nanosheets on graphene and also enhances the crystallization of Ni(OH)$_2$. Many functional groups of GO (hydroxyl, epoxy, carboxyl and carbonyl groups) act as anchor sites for growth. This novel Ni(OH)$_2$/graphene composite inherits the advantages of graphene nanosheets and two-dimensional Ni(OH)$_2$ materials thus exhibit higher specific capacitance, better rate capability and cycling stability compared to pure Ni (OH)$_2$. The obtained novel Ni(OH)$_2$/GS hybrid with optimization ratio holds high specific capacitance and excellent cycling stability up to 6000 cycles even at a high scan rate of 50 mV s^{-1}. The significant improvement is rarely reported in previous literatures and is attributed to its tailored properties, which are vital to the operation of SCs, including the intimate bindings, high conductivity, structural stability, and good wettability. It is concluded that the synergetic effect between graphene and two-dimensional Ni(OH)$_2$ structure benefits the improvement of the electrochemical properties of the hybrid composites. This facile method may offer an attractive alternative approach for preparation of the graphene based two-dimensional composites as high performance electrodes for super-capacitors.

Methods

Synthesis of graphene oxide. Graphene oxide was prepared by the oxidation of natural graphite powder via an improved Hummers method[42]. Briefly, a 9 : 1 mixture of concentrated H$_2$SO$_4$/H$_3$PO$_4$ (45 : 5 mL) was added to a mixture of graphite flakes (0.375 g) and KMnO$_4$ (2.25 g). The reaction was then heated to 50°C and stirred for 24 h. The reaction was cooled to room temperature and poured onto ice (200 mL) with 30% H$_2$O$_2$ (3 mL). Then, the mixture was centrifuged (10000 rpm for 5 min). The remaining solid material was then washed in succession with 200 mL of 30% HCl for twice, and 400 mL of water for three times. For each wash, the mixture was centrifuged (12000 rpm for 10 min) and graphite oxide was obtained. The as-prepared graphite oxide was dispersed into deionized water to form a homogenous solution (about 1 mg mL^{-1}).

Synthesis of precursor Ni(OH)$_2$. NiSO$_4$·7H$_2$O (2.5759 g) and NaOH (0.132 g) was dissolved in 100 mL deionized water and stirred for 30 min. Then we obtained precursor Ni(OH)$_2$ precipitation by centrifuging and washing the mixture with copious deionized water for several times.

Synthesis of pure Ni(OH)$_2$. The as-obtained Ni(OH)$_2$ precursor particles were dispersed into 150 mL DMF, and sonicated for 60 min to separate stacked precursors and thereafter are used for refluxing at 95°C for 16 h.

Synthesis of Ni(OH)$_2$/GS composites. The as-obtained Ni(OH)$_2$ precursors were dispersed into deionized water, and then different amount of GO was added. The ratio of GO to Ni(OH)$_2$ is 1 : 20, 1 : 5, and 1 : 2 by mass. After stirring and sonicating for 60 min to separate stacked precursors, the precursor was first deposited on GO uniformly in aqueous solution. And then the intermediate products were centrifuged with deionized water, and dispersed into 150 mL DMF for refluxing at 95°C for 16 h. Ni(OH)$_2$/GS composites were obtained by centrifuging and washing the mixture with copious de-ionized water and ethanol for several times and then collected by lyophilization.

Materials characterization. X-ray diffraction (XRD) patterns were collected on Bruker D8 Focus Powder X-ray diffractometer using Cu Kα radiation (40 kV, 40 mA). The scanning electron microscopy was performed by using a field emission scanning electron microscopy (FESEM, HITACHI, S-4800). Transmission electron

microscopy (TEM), high-resolution transmission electron microscopy (HTEM), scanning transmission electron microscopy (STEM) and energy dispersive X-ray spectroscopy mapping technique were taken on a FEI Tacnai G2 electron microscope operated at 200 kV. X-Ray photoelectron spectrometry data was acquired using an ESCALAB X-ray photoelectron spectrometer with monochromatic Al Kα X-rays. Zeta potential (ζ, effective surface charge) was measured by dynamic light scattering (Malvern Nano-ZS, UK). Raman spectra were collected with a Renishaw 1000 model confocal microscopy Raman spectrometer with a CCD detector and a holographic notch filter at ambient conditions. The specific surface area and porosity were determined by nitrogen sorption using a Micrometritics ASAP 2020 analyzer. Specific surface areas were calculated by the Brunaure-Emmert-Teller (BET) method. Pore volumes and sizes were estimated from pore size distribution curves from the adsorption isotherms using the Barrett-Joyner-Halenda (BJH) method. Thermogravimetric analysis (TGA) was performed at a heating rate of 5°C/min in flowing air (NETZSCH STA 449 F3, Germany).

Preparation of the electrodes. To evaluate the electrochemical properties of pure $Ni(OH)_2$ and $Ni(OH)_2$/GS composites, working electrodes were prepared by mixing the as-obtained powder (80 wt%) as active material with acetylene black (10 wt%) and PTFE (10 wt%). The mixtures were grounded in alcohol and the obtained slurries were pasted and pressed onto a nickel foam substrate at 10 MPa and then dried at 80°C overnight. The mass of the active materials was about 1.5 mg. Before testing, the electrode materials should be activated for abundant cycles until they can stabilizes at a certain condition.

Electrochemical evaluation. The electrochemical measurements were carried out using a three-electrode mode in 6 M KOH aqueous solution. Hg/HgO electrode filled with 1 M KOH was used as reference electrode, and a platinum plate was used as counter electrode. Electrochemical studies including cyclic voltammetry (CV), galvanostatic charge-discharge (GC) and electrochemical impedance spectroscopy (EIS) were carried out using VMP3 electrochemical workstation (Bio-logic Inc.). All tests were performed at room temperature. Typical CV curves were measured at different scan rates from 2 to 200 mV s^{-1} between 0.1 and 0.6 V. GC measurements were conducted under various current densities from 1 to 100 A g^{-1} between 0.0 and 0.5 V. EIS tests were performed for the working electrode in a frequency range of 100 kHz–0.01 Hz with ac perturbation of 5 mV. The EIS data were analyzed using Nyquist plots, which represent the imaginary part (Z″) and real part (Z′) of impedance.

1. Chmiola, J. *et al.* Anomalous increase in carbon capacitance at pore sizes less than 1 nanometer. *Science* **313**, 1760–1763 (2006).
2. Miller, J. R. & Simon, P. Electrochemical capacitors for energy management. *Science* **321**, 651–652 (2008).
3. Chmiola, J., Largeot, C., Taberna, P. L., Simon, P. & Gogotsi, Y. Monolithic carbide-derived carbon films for micro-supercapacitors. *Science* **328**, 480–483 (2010).
4. Simon, P. & Gogotsi, Y. Materials for electrochemical capacitors. *Nat. Mater.* **7**, 845–854 (2008).
5. Stoller, M. D. & Ruoff, R. S. Best practice methods for determining an electrode material's performance for ultracapacitors. *Energy Environ. Sci.* **3**, 1294–1310 (2010).
6. Zhu, H., Wang, X., Liu, X. & Yang, X. Integrated synthesis of poly(o-phenylenediamine)-derived carbon materials for high performance supercapacitors. *Adv. Mater.* **24**, 6524–6529 (2012).
7. Liu, C., Li, F., Ma, L. P. & Cheng, H. M. Advanced materials for energy storage. *Adv. Mater.* **22**, E28–E62 (2010).
8. Guo, Y. G., Hu, J. S. & Wan, L. J. Nanostructured materials for electrochemical energy conversion and storage devices. *Adv. Mater.* **20**, 2878–2887 (2008).
9. Jiang, H., Lee, P. S. & Li, C. 3D carbon based nanostructures for advanced supercapacitors. *Energy Environ. Sci.* **6**, 41–53 (2013).
10. Choi, N. S. *et al.* Challenges facing lithium batteries and electrical double-layer capacitors. *Angew. Chem. Int. Ed.* **51**, 9994–10024 (2012).
11. Zhao, X., Sanchez, B. M., Dobson, P. J. & Grant, P. S. The role of nanomaterials in redox-based supercapacitors for next generation energy storage devices. *Nanoscale* **3**, 839–855 (2011).
12. Wang, G., Zhang, L. & Zhang, J. A review of electrode materials for electrochemical supercapacitors. *Chem. Soc. Rev.* **41**, 797–828 (2012).
13. Yuan, C. *et al.* Ultrathin mesoporous NiCo$_2$O$_4$ nanosheets supported on Ni foam as advanced electrodes for supercapacitors. *Adv. Funct. Mater.* **22**, 4592–4597 (2012).
14. Jiang, J. *et al.* Large-scale uniform alpha-Co(OH)$_2$ long nanowire arrays grown on graphite as pseudocapacitor electrodes. *ACS Appl. Mater. Interfaces* **3**, 99–103 (2011).
15. Zhang, G. & Lou, X. W. Controlled growth of NiCo$_2$O$_4$ nanorods and ultrathin nanosheets on carbon nanofibers for high-performance supercapacitors. *Sci. Rep.* **3**, 1470–1475 (2013).
16. Guan, C. *et al.* Nanoporous walls on macroporous foam: rational design of electrodes to push areal pseudocapacitance. *Adv. Mater.* **24**, 4186–4190 (2012).
17. Jung, S. M., Jung, H. Y., Dresselhaus, M. S., Jung, Y. J. & Kong, J. A facile route for 3D aerogels from nanostructured 1D and 2D materials. *Sci. Rep.* **2**, 849–853 (2012).
18. Chien, H. C., Cheng, W. Y., Wang, Y. H. & Lu, S. Y. Ultrahigh specific capacitances for supercapacitors achieved by nickel cobaltite/carbon aerogel composites. *Adv. Funct. Mater.* **22**, 5038–5043 (2012).
19. Shao, M. *et al.* Core–shell layered double hydroxide microspheres with tunable interior architecture for supercapacitors. *Chem. Mater.* **24**, 1192–1197 (2012).
20. Tang, P. Y., Zhao, Y. Q., Wang, Y. M. & Xu, C. L. Metal decorated nickel foam inducing regulatable manganese dioxide nanosheet arrays architecture for high-performance supercapacitor application. *Nanoscale. DOI: 10.1039/C3NR02119J* (2013).
21. Sumboja, A., Foo, C. Y., Wang, X. & Lee, P. S. Large Areal Mass, Flexible and Free-Standing Reduced Graphene Oxide/Manganese Dioxide Paper for Asymmetric Supercapacitor Device. *Adv. Mater.* **25**, 2809–2815 (2013).
22. Chen, H., Hu, L., Yan, Y., Che, R., Chen, M. & Wu, L. One-Step Fabrication of Ultrathin Porous Nickel Hydroxide-Manganese Dioxide Hybrid Nanosheets for Supercapacitor Electrodes with Excellent Capacitive Performance. *Adv. Energy Mater. DOI: 10.1002/aenm.201300580* (2013).
23. Yang, G. W., Xu, C. L. & Li, H. L. Electrodeposited nickel hydroxide on nickel foam with ultrahigh capacitance. *Chem. Commun.* **0**, 6537–6539 (2008).
24. Wu, M. S. & Huang, K. C. Fabrication of nickel hydroxide electrodes with open-ended hexagonal nanotube arrays for high capacitance supercapacitors. *Chem. Commun.* **47**, 12122–121224 (2011).
25. Lu, Z., Chang, Z., Zhu, W. & Sun, X. Beta-phased Ni(OH)$_2$ nanowall film with reversible capacitance higher than theoretical Faradic capacitance. *Chem. Commun.* **47**, 9651–9653 (2011).
26. Jin, M. *et al.* Sponge-like Ni(OH)$_2$-NiF$_2$ composite film with excellent electrochemical performance. *Phys. Chem. Chem. Phys.* **5**, 1601–1605 (2013).
27. Zhong, J. H. *et al.* Co$_3$O$_4$/Ni(OH)$_2$ composite mesoporous nanosheet networks as a promising electrode for supercapacitor applications. *J. Mater. Chem.* **22**, 5656–5665 (2012).
28. Mohana Reddy, A. L., Gowda, S. R., Shaijumon, M. M. & Ajayan, P. M. Hybrid nanostructures for energy storage applications. *Adv. Mater.* **24**, 5045–5064 (2012).
29. Wang, Y. *et al.* High performance hybrid supercapacitor based on graphene-supported Ni(OH)$_2$-nanowites and ordered mesoporous carbon CMK-5. *J. Electrochem. Soc.* **160**, A98–A104 (2013).
30. Huang, X., Qi, X., Boey, F. & Zhang, H. Graphene-based composites. *Chem. Soc. Rev.* **41**, 666–686 (2012).
31. Stoller, M. D., Park, S., Zhu, Y., An, J. & Ruoff, R. S. Graphene-based ultracapacitors. *Nano Lett.* **8**, 3498–3502 (2008).
32. Zhang, L. *et al.* Porous 3D graphene-based bulk materials with exceptional high surface area and excellent conductivity for supercapacitors. *Sci. Rep.* **3**, 1408–1416 (2013).
33. Sheng, K., Sun, Y., Li, C., Yuan, W. & Shi, G. Ultrahigh-rate supercapacitors based on eletrochemically reduced graphene oxide for ac line-filtering. *Sci. Rep.* **2**, 247–251 (2012).
34. Lei, Z., Christov, N. & Zhao, X. S. Intercalation of mesoporous carbon spheres between reduced graphene oxide sheets for preparing high-rate supercapacitor electrodes. *Energy Environ. Sci.* **4**, 1866–1873 (2011).
35. Qu, Q., Yang, S. & Feng, X. 2D sandwich-like sheets of iron oxide grown on graphene as high energy anode material for supercapacitors. *Adv. Mater.* **23**, 5574–5580 (2011).
36. Xu, B. *et al.* What is the choice for supercapacitors: graphene or graphene oxide. *Energy Environ. Sci.* **4**, 2826–2830 (2011).
37. Tour, J. M. *et al.* Improved synthesis of graphene oxide. *Acs Nano* **4**, 4806–4814 (2010).
38. Hummers, W. S. & Offeman, R. E. Preparation of graphitic oxide. *J. Am. Chem. Soc.* **80**, 1339–1339 (1958).
39. Lee, J. W., Ahn, T., Soundararajan, D., Ko, J. M. & Kim, J. D. Non-aqueous approach to the preparation of reduced graphene oxide/alpha-Ni(OH)$_2$ hybrid composites and their high capacitance behavior. *Chem. Commun.* **47**, 6305–6307 (2011).
40. Yan, J. *et al.* Advanced asymmetric supercapacitors based on Ni(OH)$_2$/graphene and porous graphene electrodes with high energy density. *Adv. Funct. Mater.* **22**, 2632–2641 (2012).
41. Wang, H., Casalongue, H. S., Liang, Y. & Dai, H. Ni(OH)$_2$ nanoplates grown on graphene as advanced electrochemical pseudocapacitor materials. *J. Am. Chem. Soc.* **132**, 7472–7477 (2010).
42. Dong, X. C. *et al.* 3D graphene–cobalt oxide electrode for high-performance supercapacitor and enzymeless glucose detection. *ACS Nano* **6**, 3206–3213 (2012).
43. Sathiya, M., Prakash, A. S., Ramesha, K., Tarascon, J. M. & Shukla, A. K. V$_2$O$_5$-anchored carbon nanotubes for enhanced electrochemical energy storage. *J. Am. Chem. Soc.* **133**, 16291–16299 (2011).

Acknowledgments

Author contributions

Z.W. carried out the experiments and wrote the paper. Z.W., X.L.H., Z.L.W., J.J.X. and H.G.W. discussed the results. X.B.Z. supervised the research and revised the manuscript. All authors reviewed the manuscript.

Additional information

Supplementary information accompanies this paper at http://www.nature.com/scientificreports